PONTIFICIA UNIVERSIDAD CATÓLICA DEL PERÚ

FACULTAD DE CIENCIAS E INGENIERÍA

Leptonic Modeling of the Multiwavelength Spectra of Astrophysical Sources

Trabajo de investigación para obtener el grado académico de BACHILLER EN CIENCIAS CON MENCIÓN EN FÍSICA

AUTORA:

Ariadna Uxue Palomino Ylla

ASESOR:

Dr. José Luis Bazo Alba

Lima, January 13, 2021

Abstract

This work is motivated by the physical processes which take place in active galactic nuclei (AGN). They are powerful sources of radiation in a wide wavelength. To gain knowledge about these processes, multiwavelength spectral energy distributions (SED) are used. The current work uses three types of distributions applied to two blazars, a variety of AGN objects. The SED of blazars typically has a double-hump structure which can be explained in terms of two models: the hadronic and the leptonic model. A model built only by leptonic processes (in this case, inverse Compton and synchrotron) has proved to be fairly-good to explain the gamma-ray emission from most blazars. The Python package Naima restricts model parameters to find the best fit for the observed data and characterize the source by proposing processes that could take place there. The SEDs of the Mrk 421 and PKS 0537-441 blazars were modelled. The best fits obtained follows an electron differential distribution of the form of an exponential cutoff power law. They have a reduced χ^2 of 1.92 and 2.58, respectively. For the fitted model for the blazar PKS 0537-441, the radiation of the flux of photons product of the synchrotron process produces the major contribution on the inverse Compton flux.

Resumen

Este trabajo nace del interés en los procesos que tienen lugar en los núcleos activos de galaxia (AGN). Los AGN son fuentes poderosas de radiación en un amplio espectro de frecuencias. A fin de obtener información sobre estos procesos, la distribución espectral de energía (SED) para múltiples frecuencias es utilizada. El presente trabajo usa tres tipos de distribuciones aplicadas a dos blazars, un tipo de núcleos de galaxia activos. La SED de los blazars típicamente tiene una estructura de dos montículos que puede ser explicada en términos de dos modelos: hadrónico y leptónico. Un modelo puramente compuesto de procesos leptónicos (en este caso Compton inverso y sincrotrón) ha probado ser adecuado para explicar la radiación emitida por los blazars. Naima, un paquete de Python, restringe los parámetros de los modelos para hallar el mejor ajuste para los datos observados y, de ese modo, caracterizar la fuente al proponer procesos que puedan tener lugar en ella. Los SED de los blazars Mrk 421 y PKS 0537-441 son modelados. Los mejores ajustes obtenidos siguen una distribución diferencial de electrones de la forma de un *exponential cutoff power law* y tienen χ^2 reducidos de 1.92 y 2.58 respectivamente. En el caso del modelo ajustado para el blazar PKS 0537-441, la radiación del flujo de fotones producto del proceso sincrotrón produce la mayor contribución en el origen del flujo del proceso de Compton inverso.

Acknowledgements

I would like to thank my advisor, Prof. Bazo, for providing me guidance, feedback and access to equipment for this research. I am grateful to my sister Ivanna, to my good friends and colleges Cristian, Sebastián and Johann, for taking the time (and effort) to review each of my words when required, support my grumbles and providing last-minute aid. And special thanks to my mother (she makes me a cup of coffee every single day), my grandparents and Pochoclo. Lastly, I owe a very important debt to the *Fundación Educación* and PUCP for the studentships that allowed me to reach this point.

Contents

Chapter 1

Introduction

Humans have learned about the universe through light for a long time, not only by the visible light but UV, radio or gamma radiation. Observing the vast range of emissions of some astrophysical sources allows us to have a more complete image of the processes taking place in them. Because of this, there is a large number of telescopes/detectors observing different wavelength bands.

Active galactic nuclei (AGN) are extragalactic sources with a wide range of non-thermal emission and a rapid variability display (Jang & Miller, 1995). It is theorized that a massive black hole is inside each of their centres and the accretion disk that surrounds them stores the energy of accretion (Sala, Cenci, Capelo, Lupi, & Dotti, 2020). Part of that energy will be released in form of two relativistic jets that accelerate particles to very high velocities. Blazars, a class of AGN, are objects of interest because the axis of their jets points close to the line of sight of Earth. They can be classified based on the characteristics of their optical spectrum: FSRQ (flat-spectrum radio quasar), which have strong emission lines, and BL Lac (BL Lacertae object), with weak or non-existent emission lines (Margherita, 1998).

Blazars emit radiation in a wide wavelength range. They have a typical two-hump structure in their spectral energy distribution (SED): one in the low energies, radio to x-rays, and one in the high ones, GeV to TeV (Maraschi et al., 2008). The first peak is assumed to be, by

consensus (Sahu, Oliveros, & Sanabria, 2013), the product of synchrotron radiation. Depending on the frequency of the first peak, blazars can be sub-classified as low synchrotron peaked (LSP) ($\nu_{peak} \lesssim 10^{14}$ Hz), intermediate synchrotron peaked (ISP) (10^{14} Hz $\lesssim \nu_{peak} \lesssim 10^{15}$ Hz) and high synchrotron peaked (HSP) (10^{15} Hz $\lesssim \nu_{peak}$) (Abdo et al., 2010). The second peak origin is more discussed. The leptonic most presumptive option is the inverse Compton process. The hadronic type has more alternatives, some are proton synchrotron, neutral pion decay (photo-pion production or proton-proton interactions), among others.

For this work, two BL Lacs (blazars) were chosen: Mrk 421 and PKS 0537-441. The Markarian 421 (Mrk 421) is a well-studied source: numerous observation campaigns have been done over many years because it is one of the closest blazars (z = 0.031) and has a great variability across its emission wavelengths (Chakraborty, 2020). PKS 0537-441 has been observed in a long multiwavelength campaign from microwaves to γ-rays from 2008 to 2010 (D'Ammando et al., 2013a). Because of this, a large amount of density flux data of both sources is available.

To limit the scope of the research, we focus on leptonic radiation models. The Python package Naima (Zabalza, 2015) is used to fit the SED of both blazars. The theoretical modelling of the SED allows us to understand the physical processes taking place at the sources and other unknown parameters of the jet (Cerruti, Zech, Emery, & Guarin, 2017; Yamada et al., 2020; D'Ammando et al., 2013a; Cerruti, Zech, Boisson, & Inoue, 2015; Ahnen et al., 2018).

This work is structured as follows: AGN and their possible leptonic emission mechanisms are described in Chapter 2; the data used and the observatories where they were obtained are briefly addressed in Chapter 3; the Naima tools used and a brief description of the package are presented in Chapter 4; in Chapter 5 the fitting results and a brief characterization of the sources is provided, and the final discussion is given in Chapter 6.

Chapter 2

AGNs and Leptonic Emission Models

AGNs (Fig. 1) are the cores of certain types of galaxies, which present high luminosity due to non-stellar sources (Karas, Svoboda, & Zajacek, 2019). It is theorised that a supermassive black hole (SMBH) is located inside each one of these cores. The luminosity would originate by the accumulation of gas and dust on an accretion disk. The gravitational energy of all the accreted matter of the host galaxy is conserved in that disk. As the matter in the disk falls inwards, the energy transforms into heat and light (Khassen, 2010).

This compact system has a hastily variable flux. The enormous output of energy through photons occurs in a wide spectral range (Jang & Miller, 1995), unlike other galaxies, allowing a smooth multiwavelength radiation spectrum. AGNs present a strong emission in UV, specifically in the spectral range from 10 nm to 0.3 μm, called Big Blue Bump, and an emission in x-rays, which is higher than the emission of other non-AGN galaxies (Karas et al., 2019).

AGNs can form jets when the SMBH is spinning, and its disk is strongly magnetized. These jets can be collimated very narrowly and accelerate particles to high relativistic velocities (Blandford, Meier, & Readhead, 2019). AGNs can be classified by the alignment of the axis of their jets concerning to the observer. Blazars constitute a subject of interest because their jets axis are aligned close pointing to the Earth.

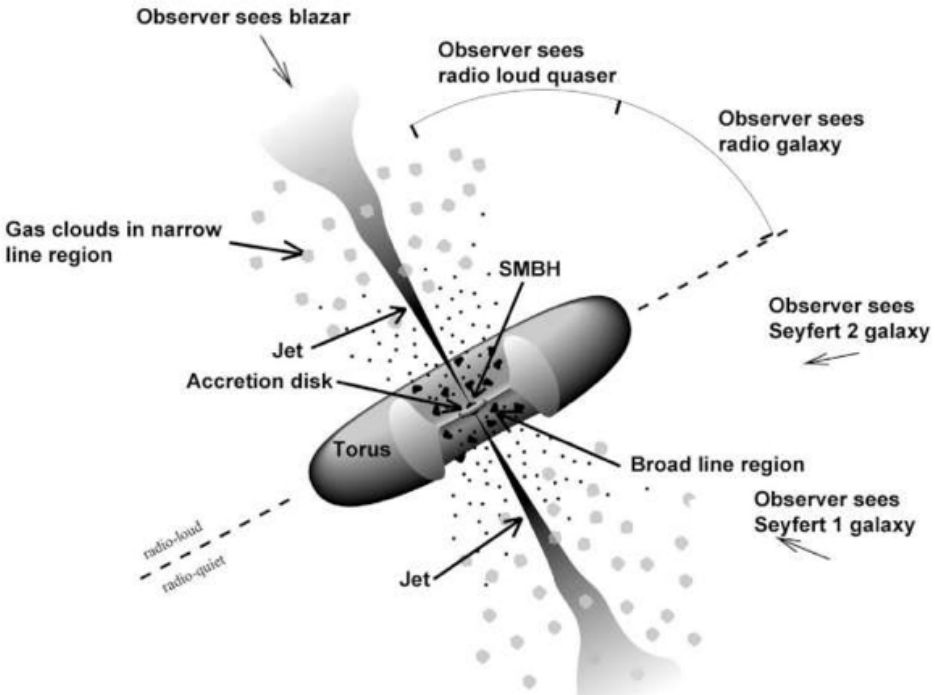

Figure 1: Active galactic nuclei structure. Figure retrieved from *Unified Model* (2016).

AGNs display variability in their spectrum, which can be referred to as flares in the SED (i.e. a rise in a part or all the flux density). Most of the studies of the variability are focused on individual sources. Flares have not a determined shape nor duration, they can last from 0.3 to 13.2 years, but they also show a correlation with frequency (Hovatta, T. et al., 2008).

The spectral energy distribution (SED) is a plot of energy E_γ [eV] vs flux density $E_\gamma^2 \frac{dN_\gamma}{dE}(E_\gamma)$ [erg s^{-1} cm^{-2}]. This last parameter refers to the amount of power radiated through an area in a frequency/energy range in the form of electromagnetic radiation or individual photons (Spurio, 2015). It is useful to characterize sources giving an idea of what processes are taking place in them and other unknown parameters of the AGNs.

The SED of blazars (see Fig. 2) has a two-hump structure. The first one happens at lower energies and it is the product of synchrotron emission. The second hump, at higher energies, can be explained by leptonic or hadronic mechanisms. In the leptonic case, it is produced by

inverse Compton scattering. The transition between these two falls in the x-ray band.

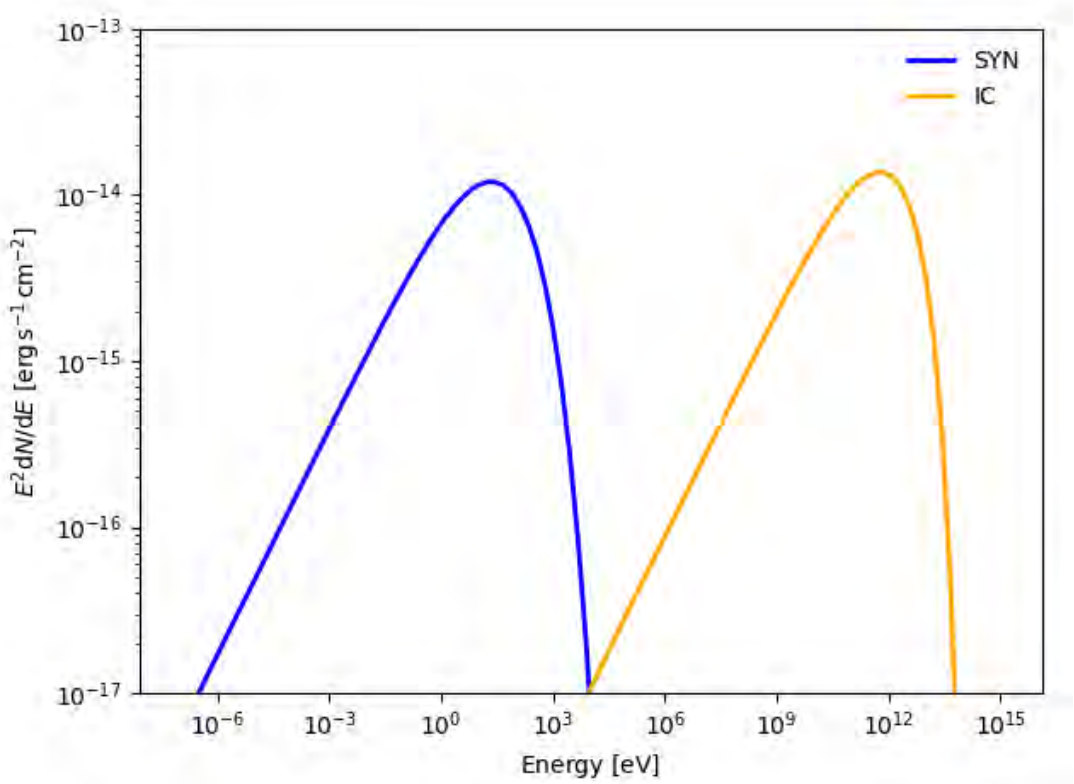

Figure 2: Spectral energy distribution of photons produced by a blazar in a leptonic model.

2.1 Synchrotron emission

Synchrotron radiation is the electromagnetic radiation generated by charged particles which are accelerated in a radial orbit (usually because of a magnetic field). It takes place in AGN jets. In this case, the emission is from non-thermal electrons or positrons. Protons can be accelerated, but they do not contribute significantly, in comparison to the electrons, to the synchrotron radiated power. The radiated power (electromagnetic radiation) for relativistic charged particles (neglecting the time dependence of the Lorentz factor Γ) is calculated from the Larmor

relativistic (v $\rightarrow$ c) formula (in c.g.s) in Spurio (2015):

$$-\frac{dE}{dt} = \frac{2q^2\Gamma^4 c}{3R^2}, \tag{2.1}$$

where q is the charge of the particle, E is its energy, c is the speed of light and R is the radius for a non-relativistic circular orbit of the particle in the magnetic field. The Lorentz factor can be expressed in terms of the energy and mass of the particle (m) that emits the electromagnetic radiation as $\Gamma = E/(mc^2)$ and, in this case (AGN), the turning radius (Gyroradius) of particles is given by the magnetic field as $r_g = R = \Gamma mc^2/(qB)$. Replacing it, we obtain:

$$-\frac{dE}{dt} = \frac{2q^4B^2E^2}{3c^7m^4}. \tag{2.2}$$

Since the mass of a proton is, approximately, 1836 times the mass of the electron, assuming they have the same particle energy, the radiated power of protons is lower than the one for electrons by fourteen orders of magnitude.

The synchrotron emission generates low energy photons with an energy spectrum peaked in the infrared/x-ray range.

2.2 Inverse Compton emission

Inverse Compton refers to the scattering of low energy photons to high energies (high x-ray to γ-ray band) at expenses of the energy of the ultra-relativistic electrons with which they interact. It is the inverse of the usual Compton scattering. The low-energy scattered photons can proceed from internal processes, as the ones produced by the synchrotron emission, or from external means to the jet (Gasparyan, 2019).

Internal processes photons refer to synchrotron photons produced inside the jet. The process which provides them is known as synchrotron self Compton (SSC) (Ghisellini, 2013). The

external processes photons can arise from other parts of the AGN, mainly from the accretion disk (optical to UV photons) (Dermer, Schlickeiser, & Mastichiadis, 1992), or from the clouds which belong to the broad-line region (optical photons) (Tavecchio & Ghisellini, 2008). External photons can also refer to infrared dust photons or cosmic microwave background photons (CMB) (Malu et al., 2017).

The radiated power of this process is given by (Spurio, 2015):

$$-\frac{dE}{dt} = \sigma_T c u'_{rad}\,, \tag{2.3}$$

where σ_T is the Thomson cross-section and u'_{rad} is the energy density of radiation in the frame of the moving electron.

In both cases, the radiated power has to be integrated over the spectrum of incident radiation and/or the spectrum of the relativistic electrons (*Inverse Compton Scattering*, 2006).

Chapter 3

Observatories and Blazar Data

The atmosphere obstructs part of the radiation in some wavelengths. This influences how the detectors are built and where they are placed. Visible light passes with little obstruction as expected. Radio wavelength radiation passes through with a minor loss, while high energy radiation (smaller wavelength than the visible range) is practically entirely blocked by the atmosphere.

3.1 Low energy observatories

Radio wavelength observatories are based on radio telescopes located on the ground. Radio telescopes can form arrays by applying interferometry to have a better definition of the radiation sources. For example, the Submillimeter Array (SMA) is an 8 telescope-array located on top of a dormant volcano in Hawaii. It operates at a frequency range from 180 GHz to 418 GHz (Ho, Moran, & Lo, 2004).

Infrared (IR) and microwave spectra are better observed from space than on Earth because the atmospheric gasses, like water vapour, absorb a large part of them. The High-Frequency Instrument (HFI) located on the space observatory Planck covered a range from 100 GHz to

857 GHz, standing mostly in the microwave spectrum (Mandolesi et al., 2004).

There are ground IR telescopes too, but they have to be located in very dry and high places to achieve minimum lost.

Visible light spectrum telescopes (or optical telescopes) can be located on ground or space and are the oldest type of telescopes (refractive telescopes). Nowadays, reflective technology is mostly used in astronomical research. The Rapid Eye Mount telescope (REM) is a robotic telescope located at the Atacama desert in Chile. The telescope has two instruments, one that operates in the near IR spectrum and a REM optical slitless spectrograph (ROSS) which covers $\sim$ 316 THz to 666 THz (Zerbi et al., 2002).

3.2 High energy observatories

Ultraviolet (UV), x-ray and γ-ray radiation are blocked by the upper atmosphere. The Neil Gehrels Swift Observatory is a NASA space observatory with three main instruments that cover from optical to x-rays: Ultraviolet/Optical Telescope (UVOT), X-ray Telescope (XRT), Burst Alert Telescope (BAT).

The UVOT, as its name states, covers part of the optical to the UV spectra. It operates from $\sim$ 0.5 PHz to 1.76 PHz (Roming et al., 2005). The XRT operates on the x-ray range, from $\sim$ 48.36 Phz to 2.42 EHz (Burrows et al., 2008). The main function of the BAT instrument is to detect and localize gamma-ray bursts (GRBs) from $\sim$ 3.63 EHz to 36.27 EHz which are located on the x-ray hard range (Barthelmy et al., 2005).

γ-rays are very energetic photons. The Fermi Gamma-ray Space Telescope (FGST) is a NASA space observatory. One of its main instruments, the Large Area Telescope (LAT), has as a primary goal to observe the gamma-ray sky to understand its sources. It operates on a wide range from $\sim$ 1.93 EHz to 72.54 YHz (Atwood et al., 2009).

Another important observatory is the Major Atmospheric Gamma Imaging Cherenkov tele-

scope (MAGIC). Unlike the Fermi telescope, it is located on the ground, but it does not work directly with gamma-ray radiation. It detects Cherenkov radiation of very high energy particle showers produced by the interaction between γ-rays and nuclei in the atmosphere. Externally works as a reflective telescope, using mirrors to concentrate the light (Lorenz & Martinez, 2005).

3.3 Markarian 421 and PKS 0537-441

The two sources analyzed in this work are Mrk 421, a high-synchrotron-peaked (HSP) BL Lac (Wakely & Horan, 2008), and PKS 0537-441, a low-synchrotron-peaked BL Lac (D'Ammando et al., 2013a).

The blazar Markarian 421 shows a highly variable flow. Between November 2004 and April 2005, a clear correlation, based on simultaneous observations, between γ-rays and x-rays was seen but not a significant one between γ-rays and lower energies. In the same work, it is mentioned that the spectrum distribution between 100 GeV to 3 TeV shows a clear (source inherent) deviation from a typical power law, with the best-fit pointing to an exponential cutoff power law (Albert et al., 2007).

The data used in this work was obtained through a campaign between January 19 to June 1, 2009, as seen in Figure 3 (Cerruti et al., 2015). An extensive part of this data comes from the Swift observatory, the MAGIC telescope and the Fermi experiment. Over this campaign, the source displayed a low activity at all observed frequencies (radio to TeV) in comparison to the flaring state it has shown in June 2008 (Abdo et al., 2011).

The blazar PKS 0537-441 presents a low-energy peak at frequencies around $\sim 10^{13}$-10^{14} Hz and a high-energy peak at frequencies around $\sim 10^{21}$-10^{22} Hz in most activity states. Data of PKS 0537-441 in this work was obtained between February and April 2010, when the blazar was in a high activity state (the blue data in Figure 4). In this state, a spectral break in the

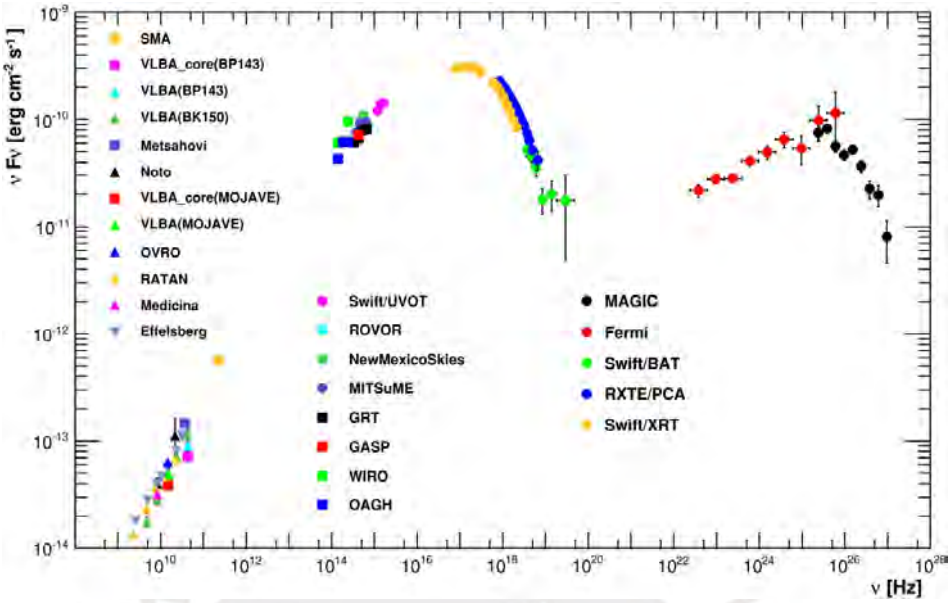

Figure 3: SED of Mrk 421 with all the observatories that collaborated during the multifrequency campaign from January 19th to June 1st, 2009. Figure retrieved from Abdo et al. (2011).

IR-optical spectrum $\sim 3 \times 10^{14}$ Hz was noticed (D'Ammando et al., 2013a).

This data was obtained from different observatories between February 28 and April 4, 2010. It was collected from REM, ATOM, Swift, LAT, Planck, WISE and the SMA observatory. The rest of the data in Figure 4, on red and black, refers to the low and average states. They were taken from separate sources over a period from February 28 to May 11, 2009, and between August 4, 2008, and February 4, 2010. All this data was collected originally in D'Ammando et al. (2013a).

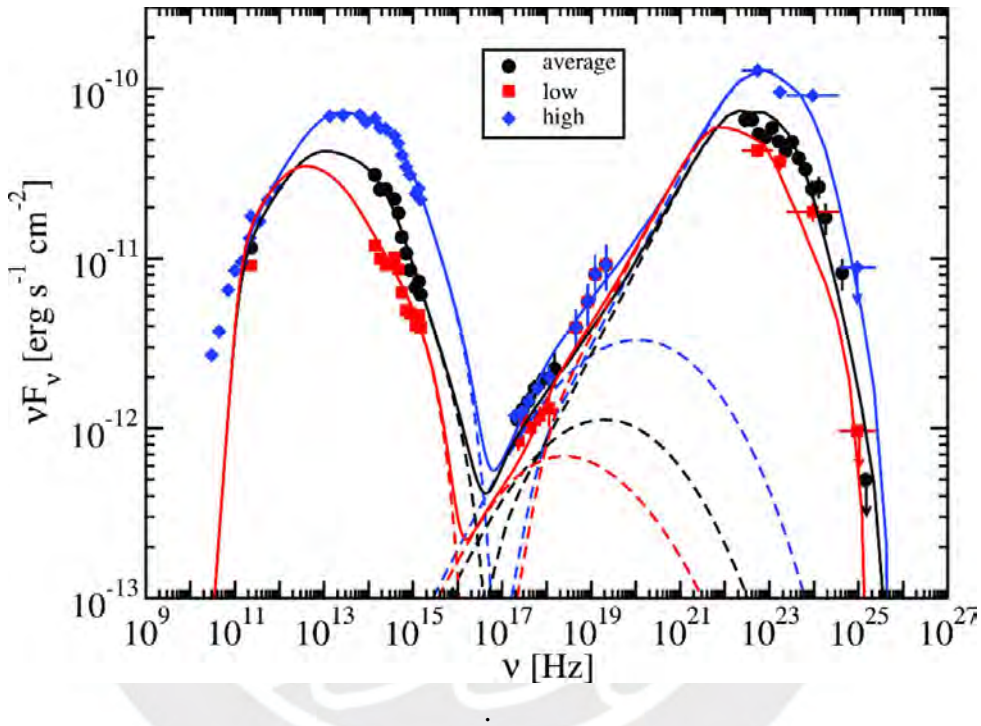

Figure 4: SED and fit of PKS 0537-441. The fit of a leptonic model with a broken power law of three parts. Figure retrieved from D'Ammando et al. (2013b).

Chapter 4

Modelling with Naima

Inside the AGN, a collection of physical processes are taking place in a wide range of physical conditions as density, pressure, the intensity of the magnetic field, among others. Extra parameters, intrinsic to the AGN, are the accretion rate and the spin of the SMBH. Idealized toy-model scenarios can reflect well the processes taking place in the AGN and their mutual exchange (Karas et al., 2019).

There are different methods to optimize the parameters which statistically best fit the data. One of these is the χ^2 minimization, but this method is not efficient by itself in this case, because the model has a large number of free parameters (Gasparyan, 2019).

Naima (Zabalza, 2015) is a Python package for modelling the non-thermal radiation from relativistic particle populations using Monte Carlo methods (based on Bayesian statistics) to fit the observed spectra. It is an efficient method for models with a large number of free parameters, as in this case.

4.1 Spectral analysis: functional forms

One of the methods to develop a model is to assume a functional form with some few free parameters. Functional forms work as spectral laws for the differential electron distribution function.

Naima includes five functional models of which we mainly use the three most used ones in previous works (Gasparyan, 2019; Tavani, Vittorini, & Cavaliere, 2015).

4.1.1 Power law

It is defined as

$$f(E) = A(E/E_0)^{-\alpha}. \tag{4.1}$$

This model has only three parameters: amplitude (A), the energy of reference or scale factor (E_0) and one exponential factor (α).

4.1.2 Broken power law

This model is a piecewise function defined by two power law functions:

$$f(E) = \begin{cases} A(E/E_0)^{-\alpha_1}, & \text{if } \mathrm{E_{break}} \geq \mathrm{E}, \\ A(E_{\mathrm{break}}/E_0)^{\alpha_2-\alpha_1}(E/E_0)^{-\alpha_2}, & \text{if } \mathrm{E} \geq \mathrm{E_{break}}. \end{cases} \tag{4.2}$$

It has five parameters: amplitude (A), the energy of reference or scale factor (E_0), two exponential factors (α_1 and α_2) and a breakpoint for the energy (E_{break}).

4.1.3 Exponential cutoff power law

This model is a power law function multiplied by an exponential term:

$$f(E) = A(E/E_0)^{-\alpha} \exp(-(E/E_{cutoff})^{\beta}). \tag{4.3}$$

It depends on five parameters: amplitude (A), the energy of reference or scale factor (E_0), exponential factors (α and β), and cutoff energy (E_{cutoff}). This model behaves like a power law until a value E_{cutoff} then drops exponentially for larger values (Milojević, 2010).

We use these models as particle distributions so the amplitude (A) must be in particles per unit energy (convertible to 1/eV).

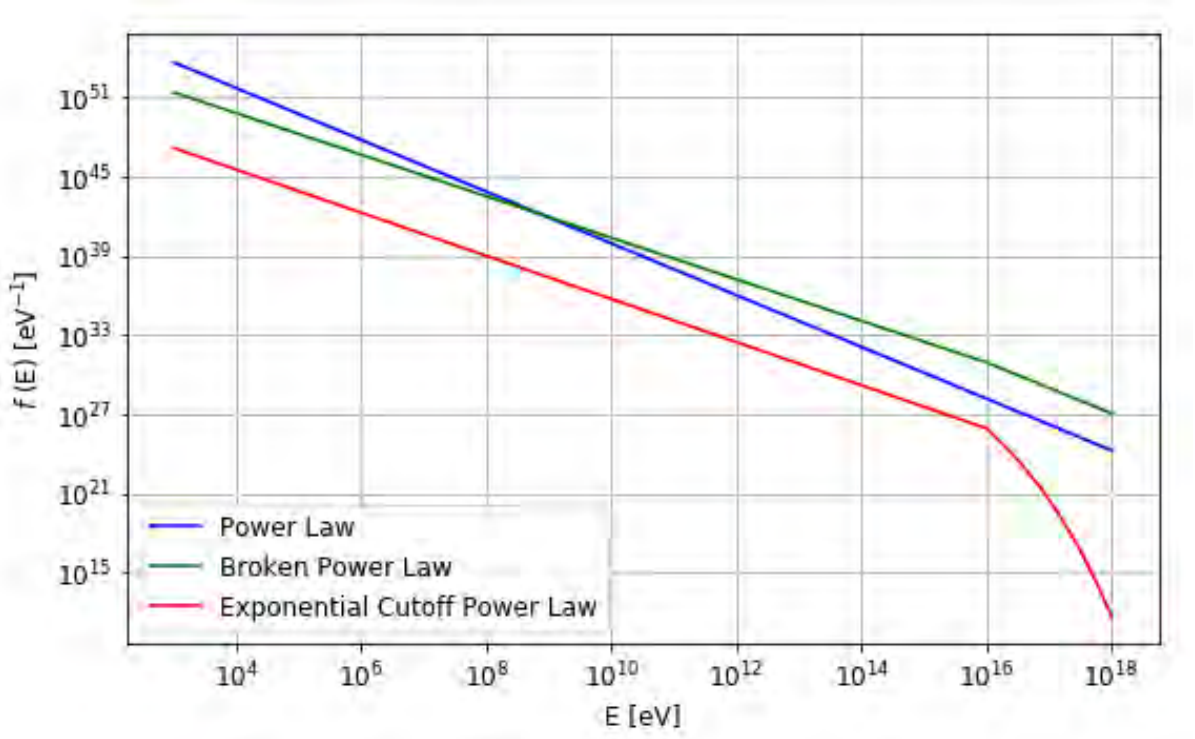

Figure 5: Examples of functional forms of the differential electron distributions for the parameters: power law (A: 6.22×10^{33} [eV^{-1}], E_0: 1.37×10^{12} [eV], α : 1.96), broken power law (A: 1.59×10^{30} [eV^{-1}], E_0: 9.38×10^{13} [eV] , α_1 : 1.93, α_2 : 1.40, E_{break}: 1.66×10^{5} [eV]) and exponential cutoff power law (A: $1.51\times10^{3}3$ [eV^{-1}], E_0: 1.91×10^{14} [eV] , α : 1.24, β : 0.26, E_{cutoff}: $10^{-0.116}$ [TeV]).

4.2 Radiative models

Naima includes four radiative models: **Synchrotron**, **Inverse Compton**, **Bremsstrahlung**, **Pion Decay**, but for the leptonic model the main ones are the first two.

4.2.1 Synchrotron

The first bump is modelled as a synchrotron process. The Naima function is based on Aharonian, Kelner, and Prosekin (2010):

$$\text{Synchrotron(particle distribution, B, E}_{emin}\text{, E}_{emax}\text{)} \ .$$

It receives an input particle distribution: one of the functional models previously mentioned, and the value of the magnetic field (B) with units. In further options, the maximum (E_{emax}) and the minimum (E_{emin}) energy of the electrons in the input particle distribution can be provided.

The original emissivity function of the synchrotron radiation (Aharonian et al., 2010) for a random magnetic fields form is

$$\frac{dN_\gamma}{dE_\gamma dt} = \frac{\sqrt{3}}{2\pi}\frac{e^3 B}{m_e c^2 \hbar E_\gamma} F\left(\frac{E_\gamma}{E_c}\right) , \tag{4.4}$$

where e is the electron charge, B is the magnetic field, m_e is the electron mass, E_γ is the gamma-ray energy, $F(x) = x\int_x^\infty K_{5/3}(\tau)\,d\tau$ ($K_{5/3}(x)$ is the modified Bessel function of the second kind and $E_c = \frac{3e\hbar B\gamma^2}{2m_e c}$ (γ is the Lorentz factor).

4.2.2 Inverse Compton

The second bump is well modelled as an inverse Compton (IC) emission. Naima uses an implementation based on Khangulyan, Aharonian, and Kelner (2014) with the following function:

$$\text{InverseCompton(particle distribution, seed photon fields, E}_{emin}\text{, E}_{emax}\text{)} \ .$$

This process also receives a functional model (the same as the synchrotron because it is the same electron distribution). For seed photon fields, it receives blackbody photon fields. In particular, Naima has CMB (cosmic microwave background), FIR (far-infrared dust emission), and NIR (near-infrared stellar emission).

In further options, the maximum (E_{emax}) and the minimum energy (E_{emin}) of the electrons in the input particle distribution can be provided.

The functions are defined for an isotropic photon field case and an anisotropic one, both cases are available in Naima (Zabalza, 2015). In this work, the isotropic case is the one used only for simplicity (Dermer, Sturner, & Schlickeiser, 1997).

The original inverse Compton emission from an electron population form (Khangulyan et al., 2014) is

$$\frac{dN_{iso}}{d\omega dt} = \frac{T^3 m_e^3 c^3 \kappa}{\pi^2 \hbar^3} \int_{\frac{\mathscr{E}_{iso}}{T}}^{\infty} \frac{d\nu_{ani/iso}}{d\omega dN_{ph} dt} \frac{x^2 dx}{e^x - 1}, \tag{4.5}$$

where ω is the energy of the scattered photon, κ is the dilution factor in the case of grey-body radiation, T is the photon gas temperature, t is defined as $t = 4ET$, where E is the energy of the electron, and $\mathscr{E}_{iso}$ is the lower limit of integration defined as $\mathscr{E}_{iso} = \frac{\omega}{4E} \frac{1}{(E-\omega)} \frac{1}{1-cos\theta}$. In the case of an isotropic target photon field, part of the integrand is defined as

$$\frac{d\nu_{iso}}{d_\omega dN_{ph} dt} = c \int (1 - cos\theta) \frac{d\sigma}{d\omega} \frac{d\Omega}{4\pi}, \tag{4.6}$$

where θ is the angle which the velocity of an electron makes with the photon's fixed direction and σ is the Lorentz-invariant cross-section for Compton scattering.

To use the radiation result from the synchrotron model as a seed photon field, it is necessary to compute the resulting radiation from a particle population and then pass it as one of the seed photon fields.

4.3 Synchrotron Self-Compton code

A critical part of the code is how to pass the radiation resultant from the synchrotron spectrum as a seed photon field to the inverse Compton.

To compute the synchrotron photon density at the source, it is needed to set a source volume and an energy array for computing the seed photon field. Then, the energy array is given as an input to the synchrotron model producing the flux as an output and then dividing it by the volume. To avoid further calculation, a spherical source is recommended: $4\pi R^2 c$ (Zabalza, 2015).

4.4 Goodness of the fit

Naima uses Markov Chain Monte Carlo to derive the best-fit model and uncertainty distributions under the assumption that the measurements and uncertainties in the provided spectrum are correct, Gaussian, and independent.

The likelihood function of the observed data given the spectral model S($\vec{p}$;E), for a parameter vector $\vec{p}$ (e.g. $\vec{p}$=('norm','index','log10(cutoff)','B')), is

$$\mathscr{L} = \prod_{i=1}^{N} \frac{1}{\sqrt{2\pi\sigma_i^2}} \exp\left(-\frac{(S(\vec{p};E_i) - F_i)^2}{2\sigma_i^2}\right), \tag{4.7}$$

where (F_i, σ_i) are the flux measurement and uncertainty at an energy E_i over N measurements (Zabalza, 2015).

The $\mathscr{L}$ function in this approximation is related to the χ^2 parameter by $\chi^2 = -2\ln(\mathscr{L})$, so that the maximization of the log-likelihood is equivalent to a minimization of χ^2.

Another method to calculate χ^2 is to consider its definition by comparing the final SED

result with the data:

$$\chi^2 = \sum_{n=1}^{N} \left(\frac{S(\vec{p}; E_i) - F_i}{\sigma_i} \right)^2, \tag{4.8}$$

which in practice gives similar results.

Chapter 5

Results and Discussion

The three functional forms mentioned in section 3 for the electron energy distribution in AGNs are tested. The number of parameters to fit depends on the election of the functional form.

A starting variation of the initial parameters is made to find the best fit. Not all parameters are varied because that would result in a large number of combinations. In particular, the initial value of the intensity of the magnetic field is obtained by a Naima function (naima.estimate_B). The other parameters were chosen from the optimization of a first run of the test. Minimum 3 parameters are picked to vary. The most influential parameters are chosen for this, as the norm or amplitude.

In the case of the power law function, the exponential factor and the energy of reference are varied. For the broken power law case, as it is a piecewise function, both exponential factors are equally important and both are taken into consideration, as the break energy. The exponential cutoff power law has two exponential factors: alpha and beta. This last parameter has a default value of 1, but in some examples of Naima, it is set as 2. In practice, a little variation of beta does not generate large changes in the final fit. This is why this parameter is not considered in the initial variation. The energy of reference was also taken into account to variate. This gives 3 initial parameters to variate in the case of power law and exponential cutoff power law, and 4

initial parameters as in Table 1 for the broken power law case. Because of this, the exponential cutoff power-law models have more combinations.

Another point is the background radiation photon fields: CMB, NIR and FIR. They can be fully specified for the IC process by giving their temperature and energy densities, but these values at the sources were not obtained. So their values are estimated within the fitting process.

Table 1: Ranges in which initial parameters vary

Power law				
Parameter	Amplitude [eV^{-1}]	E_0 [TeV]	alpha	
Range	[1e29, 1e33]	[5, 30]	[-1.89, 3.11]	
Broken power law				
Parameter	Amplitude [eV^{-1}]	E_{break} [eV]	alpha	beta
Range	[1e30, 1e34]	[1e5, 1e9]	[-1.89, 1.11]	[-1.89, 1.11]
Exponential cutoff power law				
Parameter	Amplitude [eV^{-1}]	Log(E_{cutoff} [TeV])	alpha	
Range	[1e30, 1e34]	[-4, 1]	[-1.89, 2.11]	

In all the attempts of the fitting, some of the initial values produce a (negative) large value of the likelihood function. Those were discarded by the program before further fitting.

Fitting has been attempted with all these previous considerations for both sources. Not all the resulting adjustments adequately represent the data. In this work, all the results are displayed with an emphasis on the best fit.

5.1 Mrk 421

The modelling of the spectral energy distribution of the observations taken during the multi-wavelength campaign from January 19 to June 1, 2009, of Mrk 421 (Cerruti et al., 2015) has been performed computationally.

5.1.1 Power law

Summary of results

This work tests 72 combinations of the initial parameters, 59 were successfully fitted. In Figure 6, the combinations for the first three parameters (norm, alpha and reference energy) are given. The thicker lines separate sections where the norm is constant between 10^{29} eV^{-1} (group 1), 10^{31} eV^{-1} (group 2) and 10^{33} eV^{-1} (group 3). Sections separated by dashed lines have a constant value of alpha from -1.89 to 3.11 in steps of 1 (subgroups from A to D) as stated in Table 1. Between these last sections, the energy of reference changes from 5 TeV to 30 TeV in steps size of 5 TeV. Other parameters, given in Table 2, were the same for all combinations.

Table 2: Initial values of the rest of the fitted parameters for the Mrk 421 model with a power law functional form

Parameter	Initial Value
B[μG]	13.5
T_{NIR}[K]	54.8
ρ_{NIR}[eV cm^{-3}]	0.121
T_{FIR}[K]	0.0147
ρ_{FIR}[eV cm^{-3}]	0.0338
E_{emax}[eV]	3.42e+12
E_{emin}[eV]	4.06e+04
Radius[pc]	0.0730

Best Result

The best result was given by the 40^{th} combination which belongs to group 2C. It has a reduced χ^2 of 11.78.

Figure 7 presents the total flux and the individual contributions of the synchrotron and the IC flux for the best fit, with all the seed photon fields that contribute: CMB, FIR, NIR and the one produced by the synchrotron radiation. The synchrotron peak model is not very well fitted in

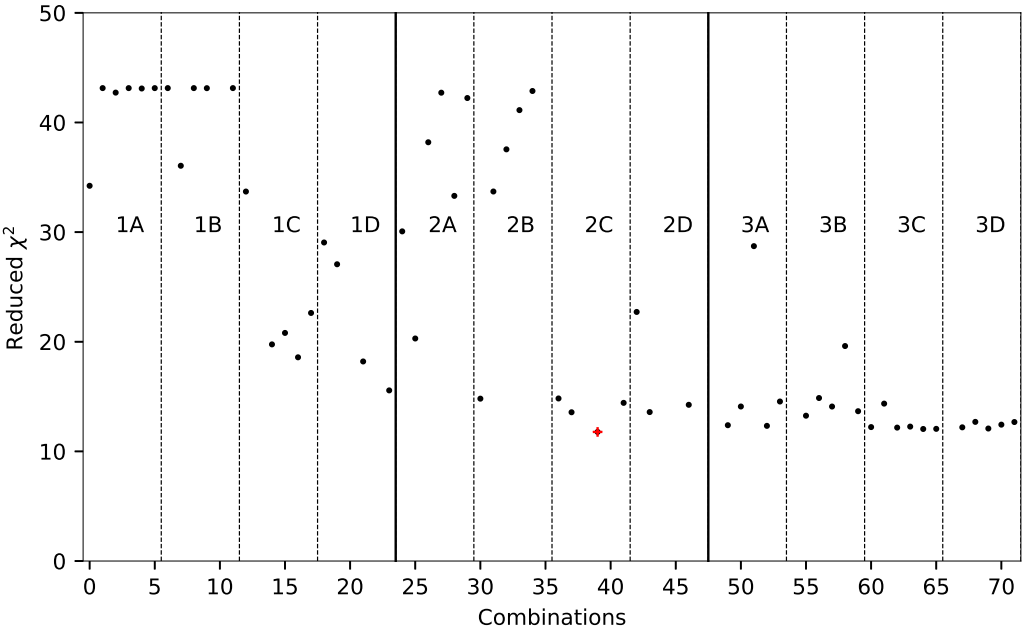

Figure 6: Reduced χ^2 calculated from the likelihood function of all tested combinations of parameters for Mrk 421 modelled with a power law. In red is the minimum χ^2.

the range of x-rays: it is higher than what the data suggests. The largest deviation in the IC one is located in the peak of the data too. The high energy hump fit has a two-peaks-form because the far-infrared contribution peak location in the energy range is far from the other background radiation peak locations.

5.1.2 Broken power law

Summary of results

This work tests 400 combinations of initial parameters. Only 328 were successfully fitted. In Figure 8, the combinations for the first three parameters (norm, alpha and break energy) are presented; the fourth parameter, beta, is not stated because it would make it difficult to read. The thicker lines separate sections where the norm is constant, it goes from 10^{30} eV^{-1} to 10^{34}

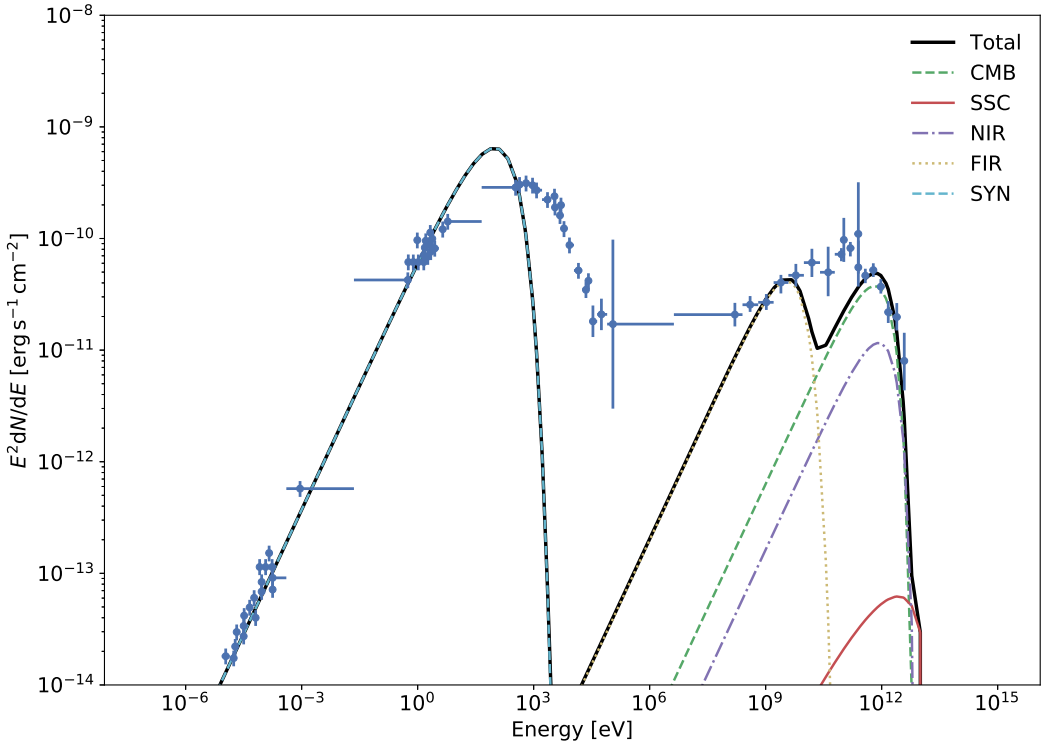

Figure 7: Best flux fit for Mrk 421 with individual components using a functional form of a power law.

eV^{-1}. The dashed lines split sections where the alpha parameter is constant from -1.89 to 1.11 in steps of 1. Other parameters, given in Table 3, were the same for all combinations.

Table 3: Initial values of the rest of the fitted parameters for the Mrk 421 model using a broken power law functional form

Parameter	Initial Value
E_0 [TeV]	60.5
B [μG]	1.35e+01
T$_{NIR}$ [K]	0.240
ρ_{NIR} [eV cm^{-3}]	0.371
T$_{FIR}$ [K]	0.00243
ρ_{FIR} [eV cm^{-3}]	0.144
E$_{emax}$ [eV]	8.00e+13
E$_{emin}$ [eV]	2.00e+04
Radius [pc]	0.800

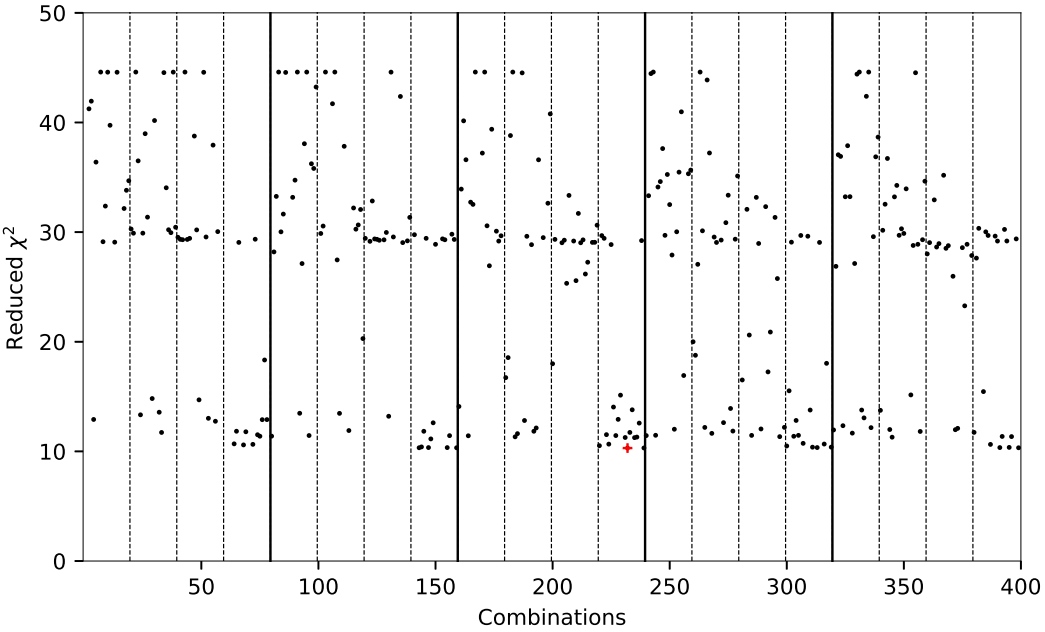

Figure 8: Reduced χ^2 calculated from the likelihood function of all tested combinations of parameters for Mrk 421 model using a broken power law. In red is the minimum χ^2.

Best Result

The best result was given by the 233^{rd} combination which belongs to the 3^{rd} value of the norm: 10^{32} eV^{-1}. It has a reduced χ^2 of 10.30.

Figure 9 presents, apart from the total flux, the individual contributions of the synchrotron and the IC flux, with all the seed photon fields that contribute: CMB, FIR, NIR and the one produced by the synchrotron radiation. The data in the synchrotron peak is not very well fitted in comparison to the IC one. The first peak fit is higher than the data flux values and far from the data in the x-ray range. The second peak fit is far from the data around 10^9 eV and 10^{11} eV.

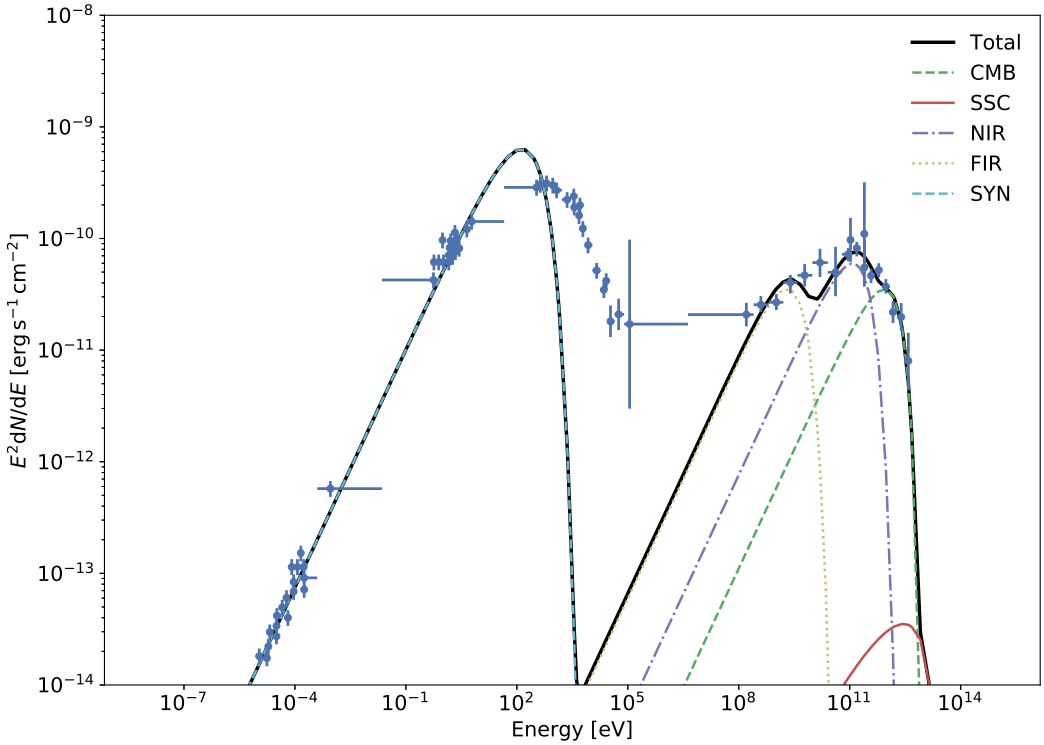

Figure 9: Best flux fit for Mrk 421 with individual components using a functional form of a broken power law.

5.1.3 Exponential cutoff power law

Summary of results

This work tests 90 combinations of initial parameters, of which 43 combinations were successfully fitted. In Figure 10, the combinations for the first three parameters (norm, alpha and cutoff energy) are displayed. The thicker lines separate sections where the norm is constant between 10^{30} eV^{-1} (group 1), 10^{32} eV^{-1} (group 2) and 10^{34} eV^{-1} (group 3). Sections separated by dashed lines have a constant value of alpha from -1.89 to 2.11 in steps of 1 (subgroups from A to E) as stated in Table 1. Between these last sections, the logarithm of the cutoff energy changes from -4 to 1 in steps size of 1. Other parameters, given in Table 4, were the same for all combinations.

Table 4: Initial values of the rest of the fitted parameters for the Mrk 421 model with an exponential cutoff power law functional form

Parameter	Initial Value
B [μG]	13.5
beta	0.280
E_{ref} [TeV]	28.0
T_{NIR} [K]	21.6
ρ_{NIR} [eV cm^{-3}]	0.0910
T_{FIR} [K]	0.0400
ρ_{FIR} [eV cm^{-3}]	0.0868
E_{emax} [eV]	4.00e+12
E_{emin} [eV]	8.00e+04
Radius [pc]	0.131

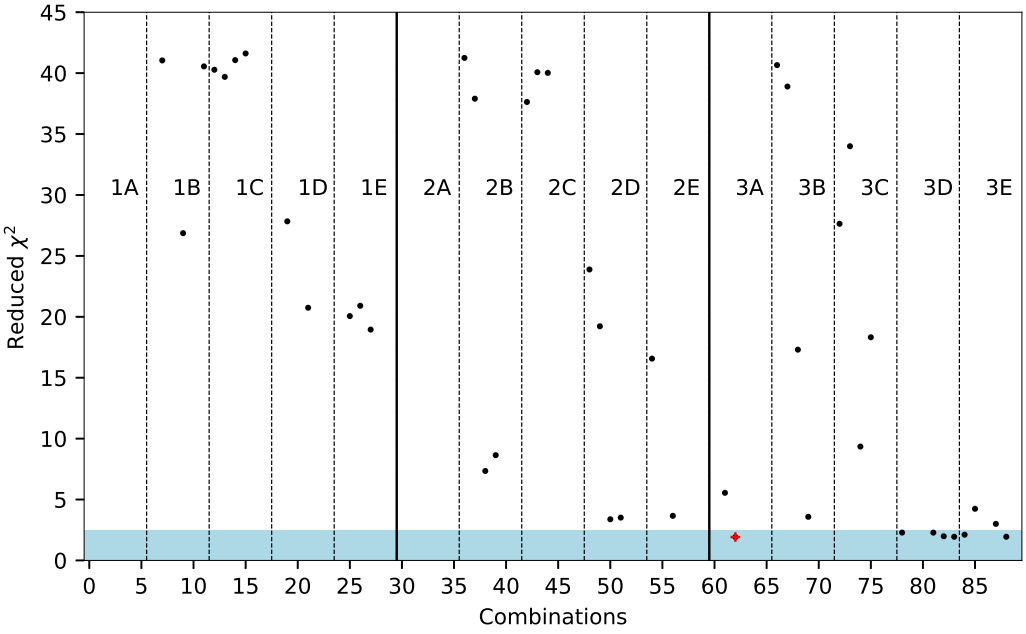

Figure 10: Reduced χ^2 calculated from the likelihood function of all tested combinations of parameters for Mrk 421 model with an exponential cutoff power law. In red is the minimum χ^2 and the sky blue section extends over values of reduced χ^2 lower than 2.5.

Best Result

The best result was given by the 63^{rd} combination, which belongs to group 3A. It presents a reduced χ^2 of 1.92.

Figure 11 displays the total flux estimated by the model, with the maximum likelihood value as a thick black line. The confidence bands at 1σ and 3σ (that represents the confidence levels) are shown in shades of grey. Below the SED is the deviation of the data concerning the maximum likelihood model. The largest data deviation from the fit occurs at the lowest energies of the synchrotron bump (microwave range).

Figure 12 presents the total flux and the individual contributions of the synchrotron and the IC fluxes. It also shows all seed photon fields that contribute: CMB, FIR, NIR and the one produced by the synchrotron radiation. The largest deviation of the IC fit from data is located around 10^8 eV and 10^{11} eV. It is seemingly smaller than the divergence in the previous functional models.

Interestingly, the best results are located all in group 3, this means all the results have a norm of 10^{34} eV^{-1}.

5.1.4 Summary of results

Table 6 is a summary of the combinations which give a reduced χ^2 lower than 2.5. In this case, all the results that accomplish this condition were obtained using an exponential cutoff power law functional.

Alpha, the electron spectral index, is the parameter with the smallest standard deviation in terms of the magnitude order of its mean. The magnitude of the magnetic field, E_{ref}, T_{FIR} and E_{emax} have a large deviation under the same evaluation.

Table 5: Four best fits for Mrk 421 with an exponential cutoff power law differential electron distribution

Combination	Group	Reduced x^2	Amplitude [eV^{-1}]	alpha	Log(E$_{cutoff}$)	B [μG]	beta	E$_{ref}$ [TeV]
62	3A	1.92	2.95e+33	1.28	3.59e-01	3.15	0.460	68.3
88	3E	1.94	1.03e+34	1.18	3.69e-04	3.38	0.411	43.4
83	3D	1.94	8.20e+33	1.29	4.36e-01	3.39	0.481	26.6
82	3D	1.98	1.38e+34	1.17	2.02e-03	2.88	0.408	42.8

Combination	T$_{NIR}$ [K]	ρ_{NIR} [eV cm^{-3}]	T$_{FIR}$ [K]	ρ_{FIR} [eV cm^{-3}]	E$_{emax}$ [eV]	E$_{emin}$ [eV]	Radius [pc]
62	11.5	0.115	5.63e-02	0.139	5.38e+12	4.47e+04	1.18e-01
88	18.9	0.149	4.00e-02	0.136	5.31e+12	1.03e+05	1.24e-01
83	10.0	0.109	8.28e-02	0.163	4.88e+12	1.06e+05	9.76e-02
82	20.5	0.140	3.38e-02	0.101	4.47e+12	7.12e+04	1.21e-01

Table 6: Estimated parameters from the best fit results of Mrk 421. These statistics were made from all fits with $\chi^2 < 2.5$. All of them were obtained with a differential electron distribution of exponential cutoff power law.

	Amplitude[eV^{-1}]	alpha	Log(E_{cutoff} [TeV])	B[μG]	beta	E_{ref} [TeV]
Mean	1.05e+34	1.20e+00	-5.93e-03	4.21	4.20e-01	3.97e+01
Mean error	1.84e+33	2.30e-02	1.09e-01	0.426	1.31e-02	5.12e+00
Standard deviation	5.19e+33	6.51e-02	3.08e-01	1.21	3.70e-02	1.45e+01
Variance error	1.44e+67	2.27e-03	5.07e-02	0.776	7.32e-04	1.12e+02
Best-Fit Value	2.95e+33	1.28e+00	3.59e-01	3.15	4.60e-01	6.83e+01

	T_{NIR} [K]	ρ_{NIR} [eV cm^{-3}]	T_{FIR} [K]	ρ_{FIR} [eV cm^{-3}]	E_{emax} [eV]	E_{emin} [eV]	Radius [pc]
Mean	3.00e+01	1.18e-01	5.57e-02	1.61e-01	6.51e+12	1.20e+05	1.19e-01
Mean error	7.00e+00	9.13e-03	7.80e-03	1.90e-02	8.20e+11	2.85e+04	1.18e-02
Standard deviation	1.98e+01	2.58e-02	2.21e-02	5.37e-02	2.32e+12	8.05e+04	3.33e-02
Variance error	2.10e+02	3.56e-04	2.60e-04	1.54e-03	2.88e+24	3.46e+09	5.94e-04
Best-Fit Value	1.15e+01	1.15e-01	5.63e-02	1.39e-01	5.38e+12	4.47+04	1.18e-01

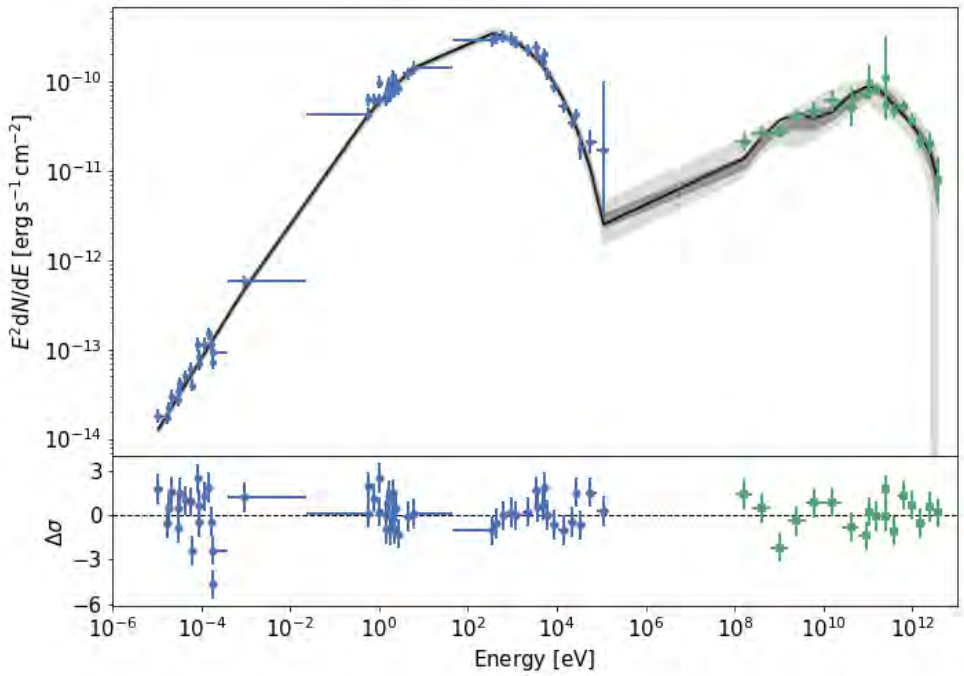

Figure 11: Best SED fit for Mrk 421 with confidence bands using an exponential cutoff power law functional form.

5.2 PKS 0537-441

The modelling of the spectral energy distribution of the observations taken during the multi-wavelength campaign from February 28 to April 4, 2010, of PKS 0537-441 is presented.

5.2.1 Power law

Summary of results

We tested 72 combinations of initial parameters, but only 12 were successfully adjusted. In Figure 13, the combinations for the first three parameters (norm, alpha and reference energy) are given. The thicker lines separate sections where the norm is constant between 10^{29} eV^{-1},

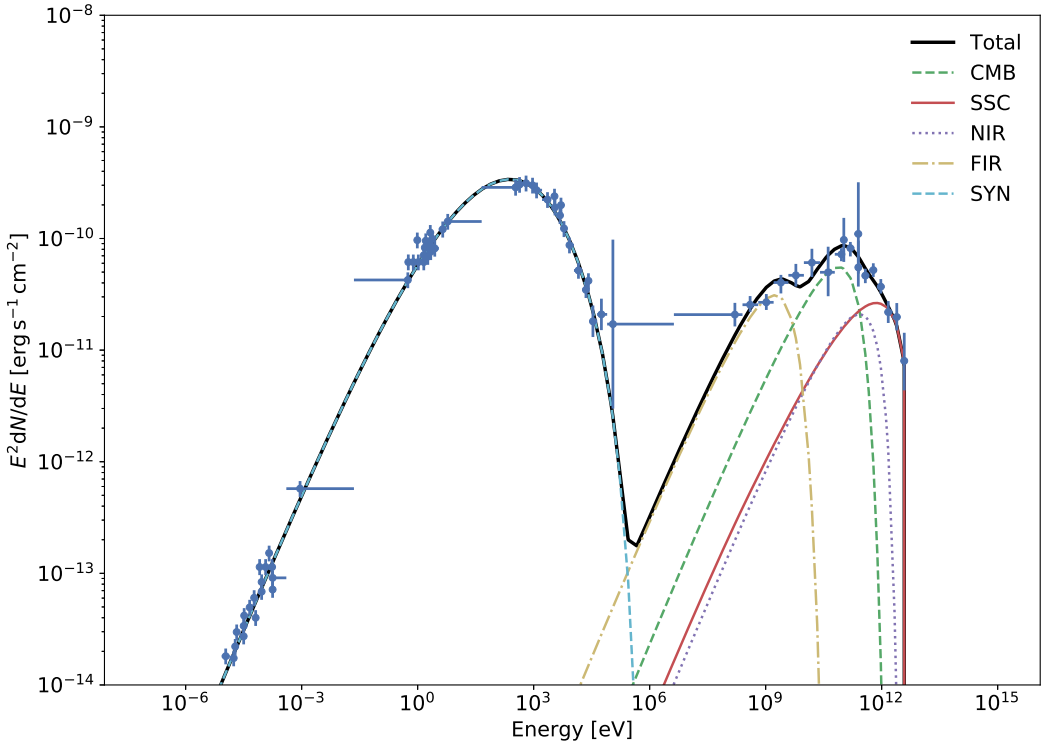

Figure 12: Best SED fit for Mrk 421 with individual components using the exponential cutoff power law functional form.

10^{31} eV^{-1} and 10^{33} eV^{-1}. Sections separated by dashed lines have a constant value of alpha from -1.89 to 3.11 in steps of 1, as stated in Table 1. Between these last sections, the energy of reference changes from 5 TeV to 30 TeV in steps size of 5 TeV. Other parameters, given in Table 7, were the same for all combinations.

Table 7: Initial values of the rest of the fitted parameters for the PKS 0537-441 model with a power law functional form

Parameter	Initial Value
B [μG]	5.27
T_{NIR} [K]	0.0402
ρ_{NIR} [eV cm^{-3}]	0.0868
T_{FIR} [K]	20.0
ρ_{FIR} [eV cm^{-3}]	0.800
E_{emax} [eV]	1.00e+12
E_{emin} [eV]	2.00e+04
Radius [pc]	0.0131

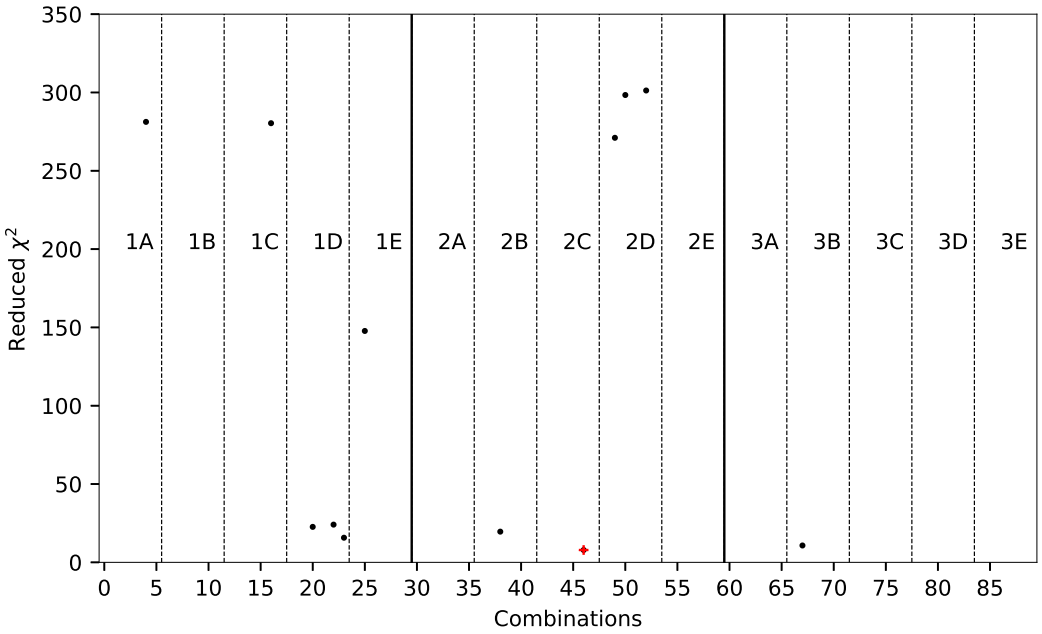

Figure 13: Reduced χ^2 calculated from the likelihood function of all the combinations of parameters for PKS 0537-441 model using a power law functional form. In red is the minimum χ^2.

Best Result

The best result was given by the 47^{th} combination which belongs to the group 2C. It presents a reduced χ^2 of 7.88.

Figure 14 displays the total flux and the individual contributions of the synchrotron and the IC flux. It also shows the seed photon fields which contribute to the IC flux: CMB, FIR, NIR and the one produced by the synchrotron radiation. This fit presents the biggest deviation from data in the left part of the synchrotron hump (in the lowest energies), and a smaller divergence at both, the synchrotron peak and the IC peak. Also, there is a deviation at the lowest energy of the given data.

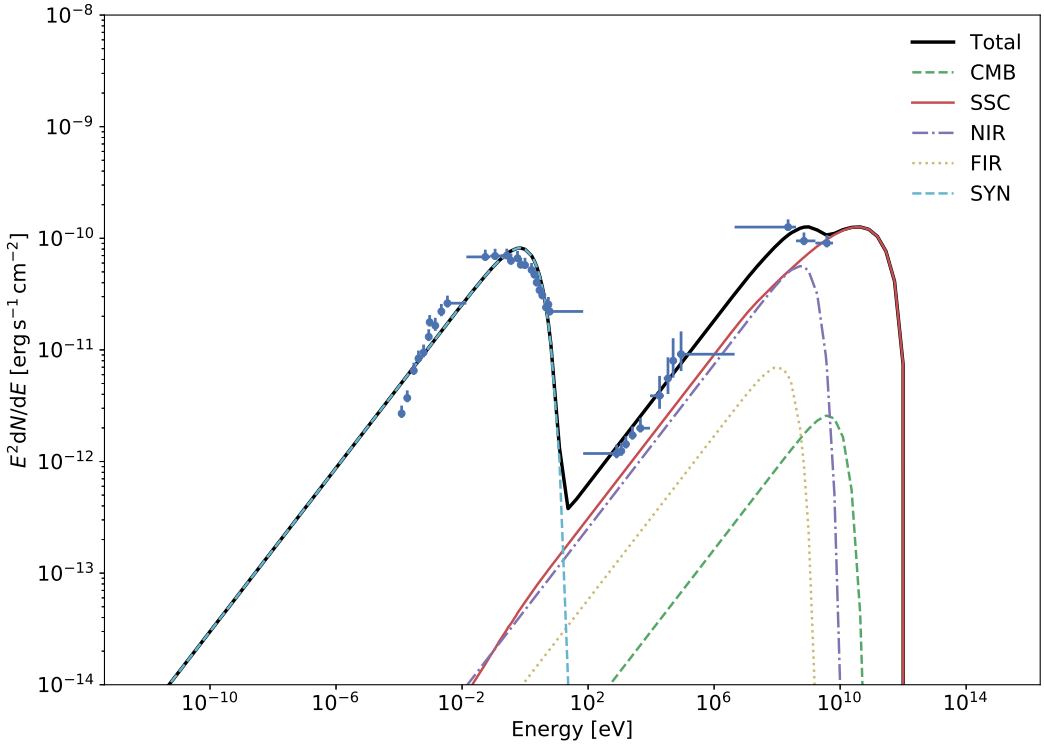

Figure 14: Best flux fit for PKS 0537-441 with individual components using a power law functional form.

5.2.2 Broken power law

Summary of results

We tested 400 combinations of initial parameters, but only 280 were successfully adjusted. As stated before, this case contains more combinations than the others. In Figure 15, the permutations for the first three parameters (norm, alpha and break energy) are displayed; the fourth parameter, beta, is not stated because it makes the picture difficult to read. The thicker lines separate sections where the norm is constant, it goes from 10^{30} eV^{-1} to 10^{34} eV^{-1}. The dashed lines split sections where the alpha is constant from -1.89 to 1.11 in steps of 1. Other parameters, given in Table 8, were the same for all combinations.

Table 8: Initial values of the rest of the fitted parameters for the PKS 0537-441 model using a broken power law functional form

Parameter	Initial Value
E_0	50.0
B [μG]	5.27
T$_{NIR}$ [K]	21.6
ρ_{NIR} [eV cm^{-3}]	0.0907
T$_{FIR}$ [K]	0.0440
ρ_{FIR} [eV cm^{-3}]	0.0868
E$_{emax}$ [eV]	9.86e+12
E$_{emin}$ [eV]	1.39e+04
Radius [pc]	1.00

Best Result

The best result was given by the 384^{th} combination which belongs to the 5^{th} value of the norm: 10^{34} eV^{-1}. It has a reduced χ^2 of 8.28. The higher energy bump is better fitted than the other.

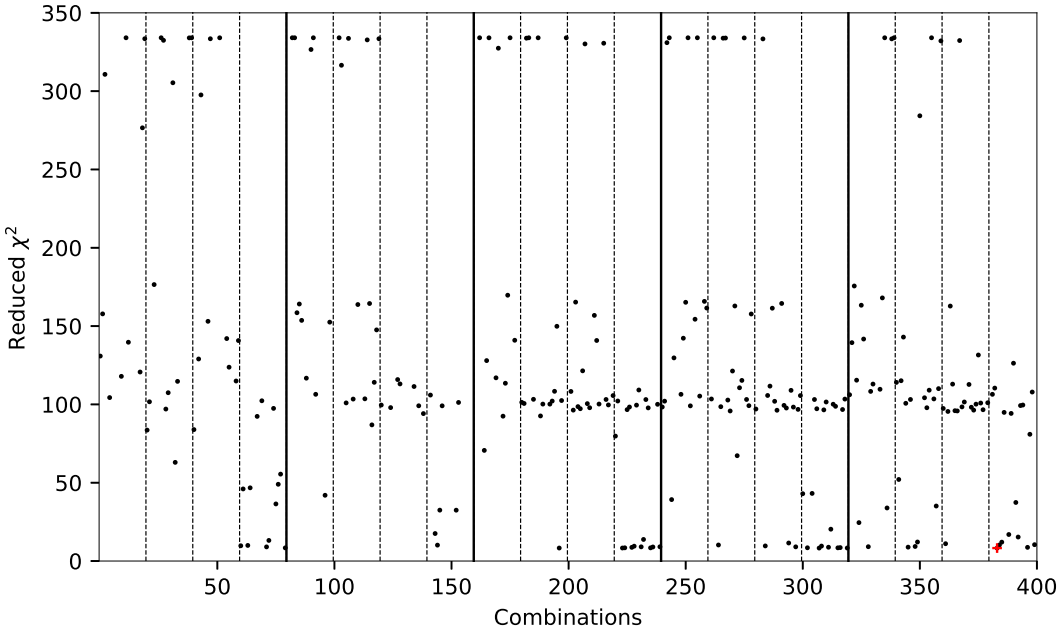

Figure 15: Reduced χ^2 calculated from the likelihood function of all tested combinations of parameters for PKS 0537-441 model with a broken power law. In red is the minimum χ^2.

5.2.3 Exponential cutoff power law

Summary of results

We tested 90 combinations of initial parameters, but only 61 were successfully adjusted. In Figure 17, the combinations for the first three parameters (norm, alpha and cutoff energy) are given.

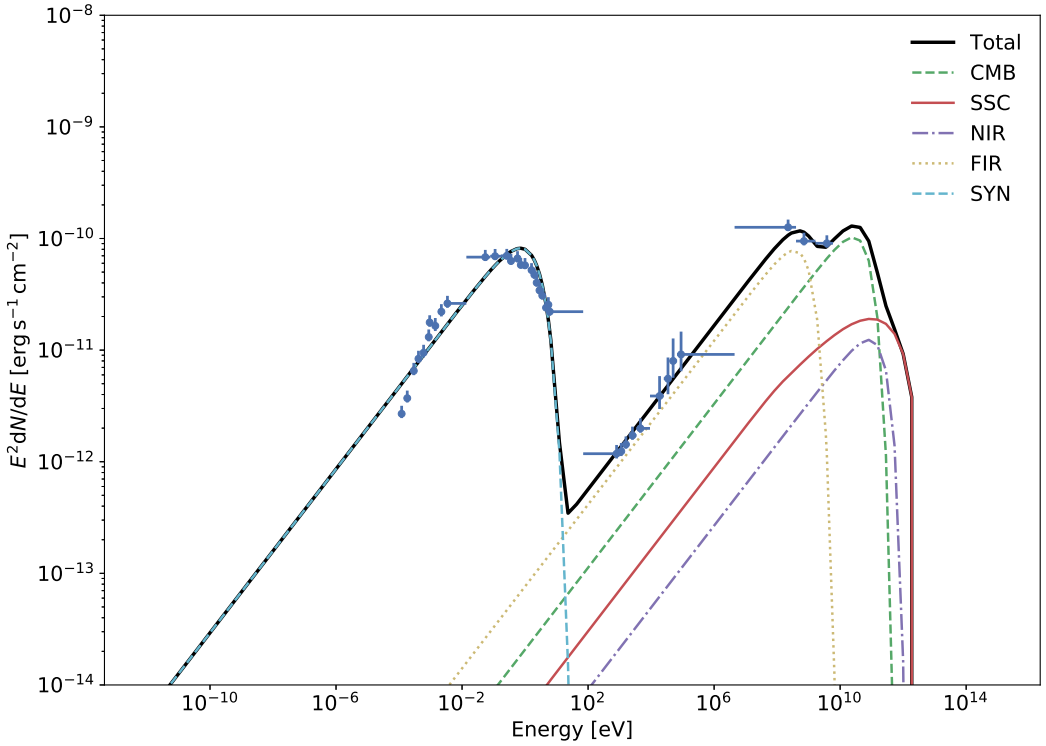

Figure 16: Best flux fit for PKS 0537-441 with individual components using a functional form of a broken power law.

Table 9: Initial values of the others fitted parameters for the PKS 0537-441 model using an exponential cutoff power law functional form

Parameter	Initial Value
B [μG]	5.28
beta	1.00
E_{ref} [TeV]	10.0
T_{NIR} [K]	0.0402
ρ_{NIR} [eV cm^{-3}]	0.0868
T_{FIR} [K]	20.0
ρ_{FIR} [eV cm^{-3}]	0.800
E_{emax} [eV]	1.00e+12
E_{emin} [eV]	2.00e+04
Radius [pc]	0.0131

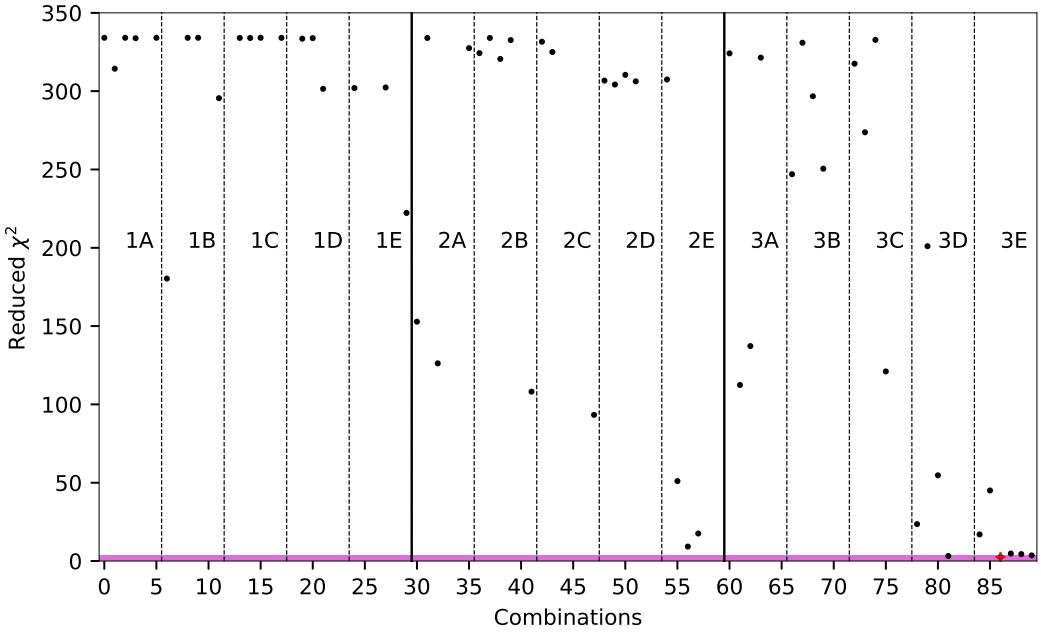

Figure 17: Reduced χ^2 calculated from the likelihood function of all the tested combinations of parameters for PKS 0537-441 model with an exponential cutoff power law. The reduced χ^2 axis is in logarithmic scale. In red is the minimum χ^2 and the magenta section extends over values of reduced χ^2 lower than 3.5.

Best Result

The best result was given by the 87^{th} combination which belongs to the group 3E. It presents a reduced χ^2 of 2.58.

Figure 18 shows the total flux estimated by the model with the maximum likelihood value as a thick black line as described before. The 3σ confidence band is wider than the one of the Mrk 421 fit. Below the SED is the deviation of the data concerning the maximum likelihood model. The largest data deviation from the fit occurs in the microwave range again. It also presents a deviation at the IC peak.

Figure 19 presents, apart from the total flux, the individual contributions of the synchrotron and the IC flux, with all the seed photon fields that contribute: CMB, FIR, NIR and the one

produced by the synchrotron radiation.

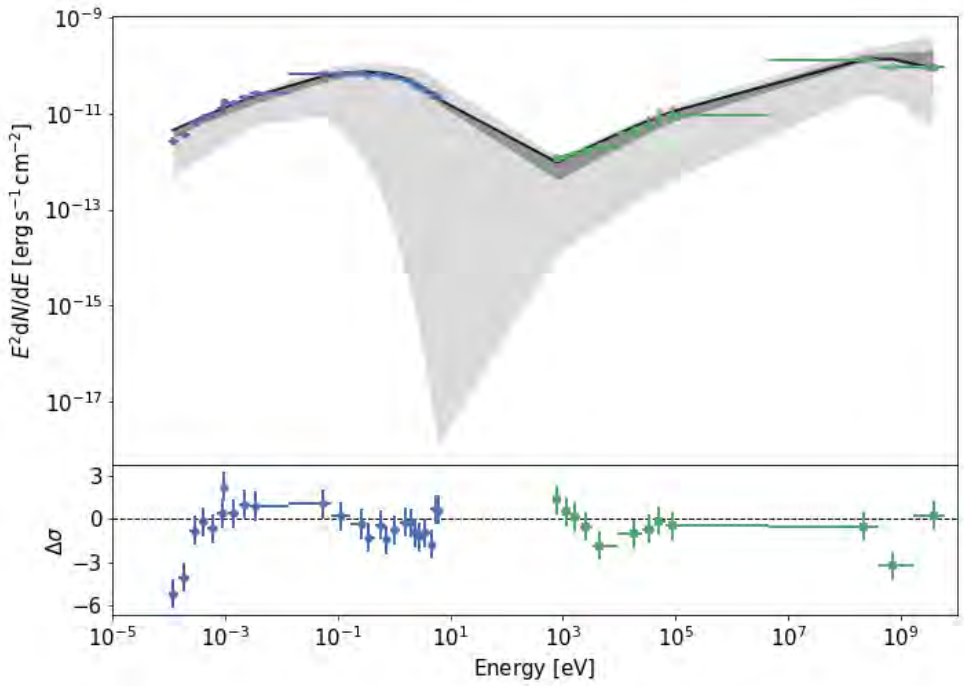

Figure 18: Best flux fit for PKS 0537-441 with confidence bands using a functional form of an exponential cutoff power law.

As in the Markarian case, the best results are located in group 3, all with a norm of 10^{34} eV^{-1}.

5.2.4 Summary of results

In this case, combinations which give a reduced χ^2 minor than 2.5 were not found. The best result was obtained by using the exponential cutoff power law functional form again. Table 6 is a summary of the combinations which give a reduced χ^2 lower than 3.5. All the results that accomplish this condition were obtained by using an exponential cutoff power law form.

The magnitude of all parameters' standard deviation is not more than one order of magnitude

Table 10: Four best fits for PKS 0537-441 with a differential electron distribution of exponential cutoff power law

Combination	Group	Reduced x^2	Amplitude [eV^{-1}]	alpha	Log(E$_{cutoff}$ [TeV])	B [μG]	beta	E$_{ref}$ [TeV]
86	3E	2.58	1.43e+34	1.82	-4.44e-01	12.2	0.715	10.3
81	3D	3.18	1.19e+34	1.77	-3.51e-01	9.03	0.765	16.0
89	3E	3.58	1.11e+34	2.03	-9.16e-03	11.5	1.19	6.19
88	3E	4.43	1.85e+33	2.08	-1.28e-03	10.7	0.934	13.6

Combination	E$_{emin}$ [eV]	E$_{emax}$ [eV]	T$_{NIR}$ [K]	ρ_{NIR} [eV cm^{-3}]	T$_{FIR}$ [K]	ρ_{FIR} [eV cm^{-3}]	Radius [pc]
86	1.44e+04	4.52e+10	1.97e-02	4.11e-02	32.0	7.51e-02	2.09e-02
81	3.57e+04	4.07e+10	8.90e-02	1.37e-01	15.7	7.10e-01	2.29e-02
89	3.29e+04	8.20e+10	8.42e-02	6.54e-02	9.63	5.27e-01	3.10e-02
88	9.00e+02	1.13e+11	4.71e-02	9.37e-03	29.8	6.98e-01	3.39e-02

Table 11: Estimated parameters from the best fitting results of PKS 0537-441. These statistics were made from all fits with $\chi^2 < 3.5$. All of them were obtained with a differential electron distribution of exponential cutoff power law.

	Amplitude[eV^{-1}]	alpha	Log(E$_{cutoff}$ [TeV])	B[μG]	beta	E$_{ref}$ [TeV]
Mean	9.54e+33	1.98	0.779	9.49	2.02	13.4
Mean error	2.82e+33	0.0759	1.06	1.04	1.21	2.49
Standard deviation	6.90e+33	0.186	2.60	2.56	2.96	6.11
Variance error	3.01e+67	0.0219	4.27	4.13	5.55	23.6
Best-Fit Value	1.43e+34	1.82	-0.444	12.2	0.715	10.3

	E$_{emin}$ [eV]	E$_{emax}$ [eV]	T$_{NIR}$ [K]	ρ_{NIR} [eV cm^{-3}]	T$_{FIR}$ [K]	ρ_{FIR} [eV cm^{-3}]	Radius [pc]
Mean	2.19e+04	8.97e+10	8.41e-02	8.71e-02	3.44e+01	1.52e+00	6.06e-02
Mean error	5.24e+03	2.14e+10	3.84e-02	2.94e-02	9.23e+00	1.05e+00	3.15e-02
Standard deviation	1.28e+04	5.24e+10	9.41e-02	7.21e-02	2.26e+01	2.58e+00	7.72e-02
Variance error	1.04e+08	1.73e+21	5.60e-03	3.28e-03	3.23e+02	4.19e+00	3.77e-03
Best-Fit Value	1.44e+04	4.52e+10	1.97e-02	4.11e-02	3.20e+01	7.51e-02	2.09e-02

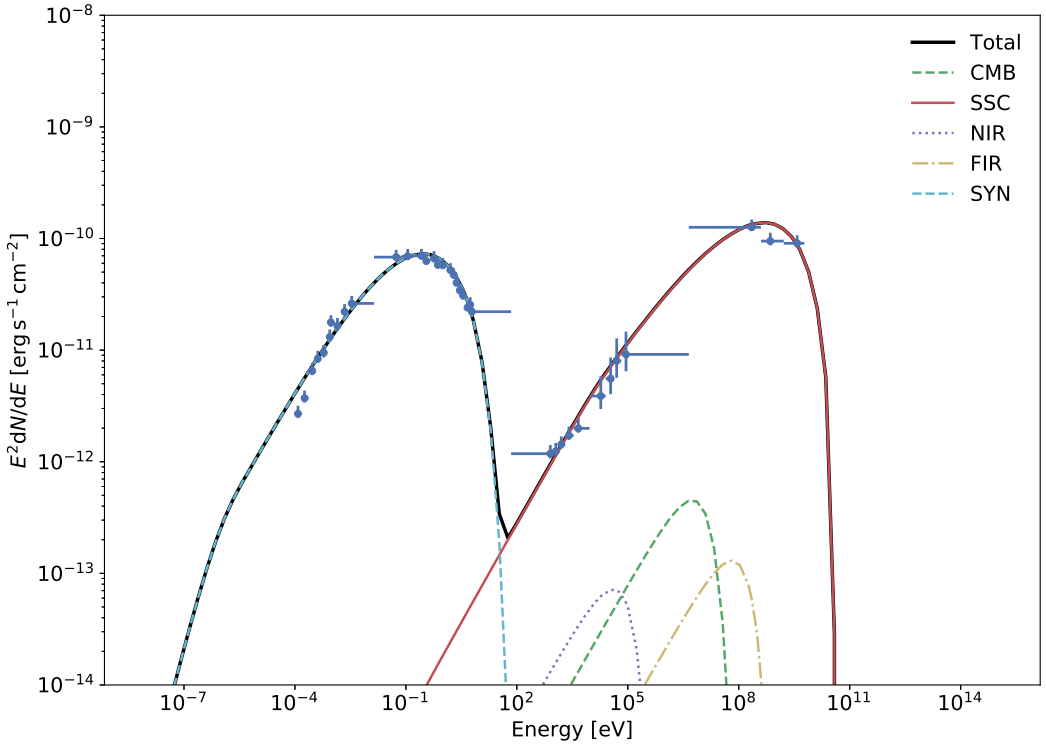

Figure 19: Best flux fit for PKS 0537-441 with individual components using a functional form of an exponential cutoff power law.

away from the mean.

Chapter 6

Conclusions

This work analyzes three differential electron functional models: power law, broken power law and exponential cutoff power law, for the leptonic model of AGNs composed of a synchrotron process for the low energy component and an inverse Compton process for the high one. The multiwavelength data of two BL Lacs blazars are discussed: Mrk 421 and PKS 0537-441. The best fits for each source are obtained with the exponential cutoff power law distribution fitted using the Naima code, with reduced χ^2 values of 1.92 and 2.58, respectively. For the first source, all sources of photon radiation for IC have meaningful contributions. For PKS 0537-441, the dominant photon radiation is obtained from the photon flux product of a previous synchrotron process. In the case of Mrk 421, this agrees with the preceding modelling of the differential electron distribution at high energies mentioned in Chapter 3. Better results in the fitting of the PKS 0537-441 have been obtained with a triple broken power law as mentioned in the same chapter. In terms of the statistics of the best fits of the Markarian blazar, alpha is the parameter with the smallest standard deviation. A coincidence in the value of the norm of the best fit results for both sources is notorious, having an amplitude of 10^{34} eV^{-1}.

References

Abdo, A. A., Ackermann, M., Agudo, I., Ajello, M., Aller, H. D., Aller, M. F., … Ziegler, M. (2010, June). The Spectral Energy Distribution of Fermi Bright Blazars. *ApJ*, *716*(1), 30-70. Doi: https://doi.org/10.1088/0004-637X/716/1/30

Abdo, A. A., Ackermann, M., Ajello, M., Baldini, L., Ballet, J., Barbiellini, G., … Zook, A. (2011, August). Fermi Large Area Telescope Observations of Markarian 421: The Missing Piece of its Spectral Energy Distribution. *ApJ*, *736*(2), 131. Doi: https://doi.org/10.1088/0004-637X/736/2/131

Abdo, A. A., Ackermann, M., Ajello, M., Baldini, L., Ballet, J., Barbiellini, G., … et al. (2011, Jul). Fermi-lat observations of markarian 421: the missing piece of its spectral energy distribution. *The Astrophysical Journal*, *736*(2), 131. Doi: http://dx.doi.org/10.1088/0004-637X/736/2/131

Abdo, A. A., Ackermann, M., Ajello, M., Baldini, L., Ballet, J., Barbiellini, G., … Zook, A. (2011). Reproduced as Figure 9 in Abdo et al. (2011).

Aharonian, F. A., Kelner, S. R., & Prosekin, A. Y. (2010, 08). Angular, spectral, and time distributions of highest energy protons and associated secondary gamma rays and neutrinos propagating through extragalactic magnetic and radiation fields. *Phys. Rev. D*, *82*(4), 043002. Doi: https://doi.org/10.1103/PhysRevD.82.043002

Ahnen, M. L., Ansoldi, S., Antonelli, L. A., Arcaro, C., Baack, D., Babić, A., … et al. (2018,

Sep). Detection of the blazar s4 0954+65 at very-high-energy with the magic telescopes during an exceptionally high optical state. *Astronomy & Astrophysics*, *617*, A30. Doi: http://dx.doi.org/10.1051/0004-6361/201832624

Albert, J., Aliu, E., Anderhub, H., Antoranz, P., Armada, A., Asensio, M., ... Zapatero, J. (2007, July). Observations of Markarian 421 with the MAGIC Telescope. *ApJ*, *663*(1), 125-138. Doi: https://doi.org/10.1086/518221

Atwood, W., Abdo, A., Ackermann, M., Althouse, W., Anderson, B., Axelsson, M., ... Ziegler, M. (2009, 05). The large area telescope on the fermi gamma-ray space telescope mission. *The Astrophysical Journal*, *697*, 1071. Doi: https://doi.org/10.1088/0004-637X/697/2/1071

Barthelmy, S. D., Barbier, L. M., Cummings, J. R., Fenimore, E. E., Gehrels, N., Hullinger, D., ... et al. (2005, Oct). The burst alert telescope (bat) on the swift midex mission. *Space Science Reviews*, *120*(3-4), 143–164. Doi: http://dx.doi.org/10.1007/s11214-005-5096-3

Blandford, R., Meier, D., & Readhead, A. (2019). Relativistic jets from active galactic nuclei. *Annual Review of Astronomy and Astrophysics*, *57*(1), 467-509. Doi: https://doi.org/10.1146/annurev-astro-081817-051948

Burrows, D. N., Kennea, J. A., Abbey, A. F., Beardmore, A., Campana, S., Capalbi, M., ... Willingale, R. (2008). *The swift x-ray telescope: Status and performance.*

Cerruti, M., Zech, A., Boisson, C., & Inoue, S. (2015, 02). A hadronic origin for ultra-high-frequency-peaked BL lac objects. *Monthly Notices of the Royal Astronomical Society*, *448*(1), 910–927. Doi: https://doi.org/10.1093/mnras/stu2691

Cerruti, M., Zech, A., Emery, G., & Guarin, D. (2017). Hadronic modeling of tev agn: Gammas and neutrinos.. Doi: https://dx.doi.org/10.1063/1.4968973

Chakraborty, N. (2020, January). Investigating Multiwavelength Lognormal-

ity with Simulations—Case of Mrk 421. *Galaxies*, *8*(1), 7. Doi: https://doi.org/10.3390/galaxies8010007

Dermer, C. D., Schlickeiser, R., & Mastichiadis, A. (1992, March). High-energy gamma radiation from extragalactic radio sources. *A&A*, *256*, L27-L30.

Dermer, C. D., Sturner, S. J., & Schlickeiser, R. (1997, mar). Nonthermal compton and synchrotron processes in the jets of active galactic nuclei. *The Astrophysical Journal Supplement Series*, *109*(1), 103–137. Doi: https://doi.org/10.1086$%$2F312972

D'Ammando, F., Antolini, E., Tosti, G., Finke, J., Ciprini, S., Larsson, S., ... et al. (2013a, Mar). Long-term monitoring of pks 0537-441 with fermi–lat and multiwavelength observations. *Monthly Notices of the Royal Astronomical Society*, *431*(3), 2481–2492. Doi: http://dx.doi.org/10.1093/mnras/stt344

D'Ammando, F., Antolini, E., Tosti, G., Finke, J., Ciprini, S., Larsson, S., ... et al. (2013b). Reproduced as Figure 10 in D'Ammando et al. (2013a).

Gasparyan, S. (2019, 04). *Modeling the multiwavelength spectra of blazars* (Vol. 12).

Ghisellini, G. (2013). Synchrotron self-compton. In *Radiative processes in high energy astrophysics* (pp. 89–93). Springer International Publishing. Doi: https://doi.org/10.1007/978-3-319-00612-3_6

Ho, P. T. P., Moran, J. M., & Lo, K. Y. (2004, Oct). The submillimeter array. *The Astrophysical Journal*, *616*(1), L1–L6. Doi: http://dx.doi.org/10.1086/423245

Hovatta, T., Nieppola, E., Tornikoski, M., Valtaoja, E., Aller, M. F., & Aller, H. D. (2008). Long-term radio variability of agn: flare characteristics. *A&A*, *485*(1), 51-61. Doi: https://doi.org/10.1051/0004-6361:200809806

Inverse compton scattering. (2006, Apr). France. Retrieved from: https://eud.gsfc.nasa.gov/Volker.Beckmann/school/download/Longair{_}Radiation3.pdf

Jang, M., & Miller, R. (1995, 09). The examination of optical microvariability in radio-quiet and radio-loud quasi-stellar objects. *The Astrophysical Journal*, *452*, 582. Doi: https://doi.org/10.1086/176330

Karas, V., Svoboda, J., & Zajacek, M. (2019). *Selected chapters on active galactic nuclei as relativistic systems.*

Khangulyan, D., Aharonian, F. A., & Kelner, S. R. (2014, 03). Simple Analytical Approximations for Treatment of Inverse Compton Scattering of Relativistic Electrons in the Blackbody Radiation Field. *ApJ*, *783*(2), 100. Doi: https://doi.org/10.1088/0004-637X/783/2/100

Khassen, Y. (2010, 10). *Active galactic nuclei.*

Lorenz, E., & Martinez, M. (2005, 12). The Magic telescope. *Astronomy & Geophysics*, *46*(6), 6.21-6.25. Doi: https://doi.org/10.1111/j.1468-4004.2005.46621.x

Malu, S., Datta, A., Colafrancesco, S., Marchegiani, P., Subrahmanyan, R., Narasimha, D., & Wieringa, M. H. (2017, December). Relativistic inverse compton scattering of photons from the early universe. *Scientific Reports*, *7*(1). Doi: https://doi.org/10.1038/s41598-017-17104-8

Mandolesi, N., Burigana, C., Butler, R. C., Cuttaia, F., De Rosa, A., Finelli, F., ... Villa, F. (2004, Nov). *The Planck Low Frequency Instrument; rev. version* (Tech. Rep. No. astro-ph/0411412). Retrieved from: https://cds.cern.ch/record/803665

Maraschi, L., Fossati, G., Tavecchio, F., Chiappetti, L., Celotti, A., Ghisellini, G., ... Takahashi, a. (2008, 12). Simultaneous x-ray and tev observations of a rapid flare from markarian 421. *The Astrophysical Journal Letters*, *526*, L81. Doi: https://doi.org/10.1086/312370

Margherita, V. R. (1998). *The deep x-ray radio blazar survey (dxrbs).*

Milojević, S. (2010, Dec). Power law distributions in information science: Making the case for logarithmic binning. *Journal of the American Society for Information Science and*

Technology, *61*(12), 2417–2425. Doi: http://dx.doi.org/10.1002/asi.21426

Roming, P. W. A., Kennedy, T. E., Mason, K. O., Nousek, J. A., Ahr, L., Bingham, R. E., ... Stock, J. (2005, Jul). The Swift Ultra-Violet/Optical Telescope. *AIP Conf. Proc.*, *727*(astro-ph/0507413), 651-654. 55 p. Retrieved from: https://cds.cern.ch/record/855552

Sahu, S., Oliveros, A. F. O., & Sanabria, J. C. (2013, May). Hadronic-origin orphan tev flare from 1es1959+650. *Physical Review D*, *87*(10). Doi: http://dx.doi.org/10.1103/PhysRevD.87.103015

Sala, L., Cenci, E., Capelo, P. R., Lupi, A., & Dotti, M. (2020). *Non-isotropic feedback from accreting spinning black holes.*

Spurio, M. (2015). *Particles and astrophysics*. Springer International Publishing. Doi: https://doi.org/10.1007/978-3-319-08051-2

Tavani, M., Vittorini, V., & Cavaliere, A. (2015, 10). An emerging class of gamma-ray flares from blazars: Beyond one-zone models. *The Astrophysical Journal*, *814*.

Tavecchio, F., & Ghisellini, G. (2008, May). The spectrum of the broad-line region and the high-energy emission of powerful blazars. *Monthly Notices of the Royal Astronomical Society*, *386*(2), 945–952. Doi: http://dx.doi.org/10.1111/j.1365-2966.2008.13072.x

Unified model. (2016). National Aeronautics and Space Administration Goddard Space Flight Center. Retrieved from: https://fermi.gsfc.nasa.gov/science/eteu/agn/

Wakely, S. P., & Horan, D. (2008, January). TeVCat: An online catalog for Very High Energy Gamma-Ray Astronomy. In *International cosmic ray conference* (Vol. 3, p. 1341-1344).

Yamada, Y., Uemura, M., Itoh, R., Fukazawa, Y., Ohno, M., & Imazato, F. (2020, May). Variations of the physical parameters of the blazar mrk 421 based on analysis of the spectral energy distributions. *Publications of the Astronomical Society of Japan*, *72*(3). Doi: http://dx.doi.org/10.1093/pasj/psaa028

Zabalza, V. (2015). naima: a python package for inference of relativistic particle energy distributions from observed nonthermal spectra. *Proc. of International Cosmic Ray Conference 2015*, 922.

Zerbi, F. M., Chincarini, G., Rodonó, M., Ghisellini, G., Antonelli, A., Conconi, P., ... Molinari, E. (2002). REM — rapid eye mount. a fast slewing robotized telescope to monitor the prompt infra-red afterglow of GRBs. In *Scientific drivers for ESO future VLT/VLTI instrumentation* (pp. 42–47). Springer Berlin Heidelberg. Doi: https://doi.org/10.1007/978-3-662-43215-0_6